Automatic T-Branch Travel of an Articulated Wheeled In-Pipe Inspection Robot Using Joint Angle Response to Environmental Changes

Atsushi Kakogawa, *Member, IEEE*, Kenya Murata, and Shugen Ma, *Fellow, IEEE*

***Abstract*—This article proposes an automatic T-branch travel method of an articulated wheeled in-pipe inspection robot, AIRo-5.2, using its joint angle response to environmental changes. The robot joints are composed of two passive elastic joints with torsional springs and a single active joint using a polyurethane-based series elastic actuator (SEA). By switching from torque control to angle control of this SEA, the AIRo-5.2 can pass through vertical T-branches. However, the timing needed to switch them has not yet been defined, and thus it was necessary to train the operators. Therefore, a method that uses the middle joint angle change was proposed for automatic T-branch travel. To elucidate the phenomenon of this angle change and to determine the effects of a robot's mechanical parameters, a partial dynamic model was constructed when only the head link contact was released at a T-branch. Finally, the travel performance of our developed in-pipe robot was tested on 10 types of T-branches with different gravity directions. From the experiments, although the probability of completing the course was not 100% in all cases, the effectiveness of our proposed principle and algorithm for automatic T-branch travel was confirmed.**

***Index Terms*—Field robots, inspection robots, mechanism design, redundant robots, search and rescue robots, torque sensor.**

I. Introduction

FUEL supply is one of the most important infrastructures in urban society, like gas and water. These facilities are often buried underground or constructed in high or narrow places, making it difficult to determine the state of deterioration inside of them. To solve this problem, robotic in-pipe inspection has been attracting increased attention, and a great deal of research and development have been conducted [1], [2].

To pass through a long, narrow, and winding pipeline, a snake-like structure is considered to be suitable, and numerous investigations related to this have already been performed. In-pipe inspection robots that incorporate this snake-like structure can be categorized into three main types. The first is a robot with a body that resembles a real snake, and moves like a snake [3], [4], [5], [6]. Since these robots do not have wheels, the overall structure can be simplified and downsized to adapt to four in diameter or less. The disadvantage, however, is that the movement speed is slow, and the robot needs to be composed of a large number of joint actuators (more than 10–20) to form a three-dimensional body shape.

The second is a robot with a worm-like peristaltic mechanism, or an expansion and contraction mechanism [7], [8], [9], [10]. Many of these robots are pneumatically driven, and the number of relevant studies has recently been increasing. Indeed, this increase may be attributable to the advantage of being able to adapt to inner diameters of 2 in or less. However, their movement speed is not as fast as that of a wheel, and it is difficult to adapt them to T-branches.

The third is a robot that combines a snake-like structure with an active wheel drive. Although the inner diameters are still limited to 3–8 in, this type of structure is the fastest and most adaptable to a variety of pipe shapes at the current stage of development. This snake- and wheel-combined structure can also be further classified into two types. The difference is whether or not the axle of the drive wheels and the axle of the joints are coaxial.

If these axes are not on the same axis, the design is straightforward [11], [12], [13], [14], [15], [16]. The overall design, however, tends to be larger. On the other hand, there are a number of reports on the coaxial arrangement of the wheel axle and joint axle because it can be downsized without compromising the in-pipe motion performance [17], [18], [19], [20], [21]. This type of robot is frequently called an articulated wheeled in-pipe inspection robot, since the drive wheels are connected by multiple joints.

However, even these existing in-pipe robots still possess certain problems, such as slow adaptation speed to T-branches, short travel distance, and an inability to pass through T-branches without fillets at the inner corners. In particular, a robot that can move freely, not only horizontally, but also vertically, through

Manuscript received 23 March 2022; revised 19 July 2022 and 12 August 2022; accepted 15 August 2022. Date of publication 25 August 2022; date of current version 17 February 2023. This work was supported by Gesuido Academic Incubation to Advanced Project (GAIA Project) of the Ministry of Land, Infrastructure, Transport and Tourism. *(Corresponding author: Shugen Ma.)*

Atsushi Kakogawa is with the Research Organization of Science and Technology, Ritsumeikan University, Kusatsu 525-8577, Japan (e-mail: kakogawa@ieee.org).

Kenya Murata and Shugen Ma are with the Department of Robotics, Faculty of Science and Engineering, Ritsumeikan University, Kusatsu 525-8577, Japan (e-mail: rr0112rk@ed.ritsumei.ac.jp; shugen@ieee.org).

This article has supplementary material provided by the authors and color versions of one or more figures available at https://doi.org/10.1109/TEM.2022.3201301.

Digital Object Identifier 10.1109/TIE.2022.3201301

Fig. 1. Overview of an in-pipe inspection robot: AIRo-5.2.

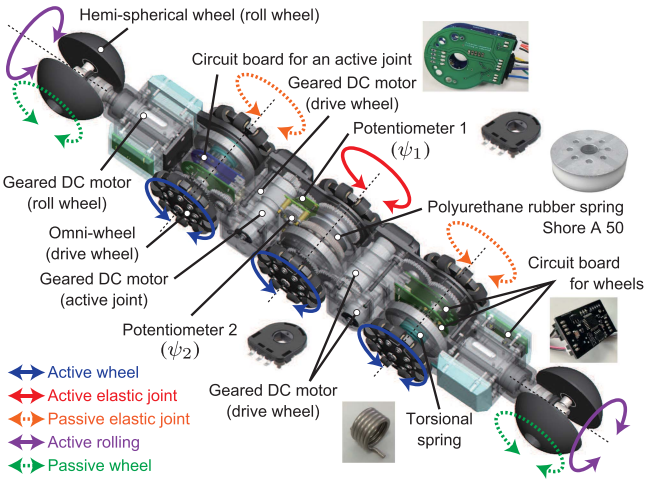

Fig. 2. CAD model of the in-pipe inspection robot AIRo-5.2.

long and narrow pipelines with an inner diameter of 4 in or less, including bent pipes with a small radius of curvature and T-shaped branches, has been a major challenge that needs to be overcome. Therefore, we assert that the following requirements should be satisfied for the development of practical in-pipe inspection robots.

1) Adaptive inner diameter of pipes should be 4 in or less.
2) The robot should pass through a T-branch in all directions at a fast speed, both horizontal and vertical (our goal is within 10 s).
3) The robot should pass through a T-branch even if its inner corner is sharp at a right angle.
4) The robot should be equipped with a mechanism to push the drive wheels against the inner wall of pipes, and can pull the cable over a long distance without slippage of the wheels.
5) The operation interface should be user-friendly.

To achieve these goals, in our previous research, we have developed an articulated wheeled in-pipe inspection robot (AIRo) [22]. Our robot is equipped with omni-wheels as the drive wheels, and spherical wheels attached to the front and rear of the robot [23], and rotates them around the linkage for rolling movement around the pipe axis. In a very recent version of our robot (AIRo-5.1) [24], only the middle one of the three joints is a torque-controllable joint with a built-in series elastic actuator (SEA) [25], [26], and the remaining two joints are passive joints with torsional springs.

It was experimentally revealed that if the angle of the middle joint is controlled along a cosine trajectory, the robot can pass through a vertical T-branch pipe, as well as a horizontal one [24]. Most recently, we have developed AIRo-5.2 (see Fig. 1), which constitutes the AIRo-5.1 with minor modifications, and it can pass through both horizontal and vertical T-branches smoothly. However, the timing for switching the control has not yet been determined, and the only way to achieve this has been for a human to switch intuitively while watching the camera image.

Therefore, in this article, a new method to switch from torque control to angle control by using the change in the angle of the middle joint at the moment that the head link of the robot breaks contact in the T-branch is proposed. To understand this phenomenon, a partial dynamic model, and the effect of the mechanical parameters of the robot for T-branch detection, are also verified. This switching method is somewhat similar to the method of using the active joint by SEA as a tactile sensor for environment recognition, and achieves automatic T-branch travel of the robot.

The contribution of this article is the realization of an in-pipe robot that can quickly travel through a 4 in T-branch pipe in any posture (regardless of horizontal and vertical directions), which was previously difficult. Moreover, the inner corners of the T-branch are sharp and bent at right angles. During the T-branch travel, the robot switches between torque control and angle control by itself without complicated manual operations. Another contribution is a partial dynamics model to theoretically derive the change in the middle joint angle, which is used for a trigger to switch the control target. The novelty of this article is that the sensors originally required for control are also applied to the identification of environmental changes.

II. Joint Structure With Angle and Torque Sensors

Our latest in-pipe inspection robot, AIRo-5.2, is a slightly modified version of the AIRo-5.1 [24]. Only the middle joint is actively driven by a SEA using polyurethane rubber spring; the other two joints are passively bent by torsional springs. These two passive joints might be replaced by the active joints. In practice, however, two additional SEAs and a transmission mechanism must be built into the rest two joints, which requires more space. Considering the space required for printed circuit board, simplified control, and motor space for roll rotation at front and rear links, the method of actively driving only the middle joint is valid and realistic.

Fig. 2 shows the CAD model of the AIRo-5.2, and Table I lists its specifications. The materials of the first and second links were changed from ABS plastic to aluminum, which made the spring fixation stronger while slightly increased the weight. The omni-wheel is specially designed to achieve durability and high friction using nitrile butadiene rubber. Spherical wheels at the head and tail of the robot are made of silicon that has been casted by hand.

In the AIRo-5.2, two potentiometers, RDC506018A (Alps Electric Co. Ltd., Tokyo, Japan), are installed as angle sensors

TABLE I
SPECIFICATIONS OF AIRO-5.2

Adaptive pipe inner diameter	4–5 in
Total length (when extended)	0.51 m
Total weight (without cable)	2.37 kg
Max. moving speed	0.08 m/s
Max. continuous traction force	202 N (20.6 kgf)
Peak traction force	808 N (82.4 kgf)
Max. continuous joint torque	3.76 Nm
Peak joint torque	15 Nm
Joint angular speed	13.6 rpm (1.43 rd/s)
Nominal voltage	DC 24 V
Communication	Controller Area Network (CAN)

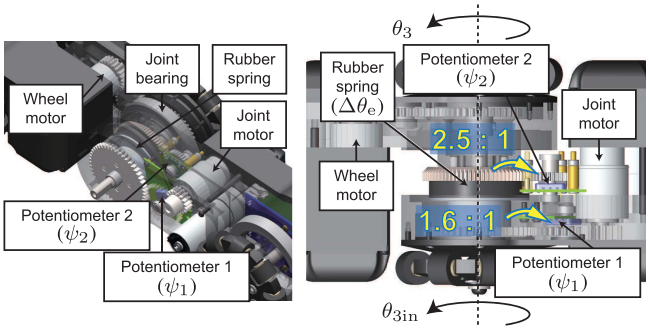

Fig. 3. Joint structure and angle sensor arrangement of the AIRo-5.2; potentiometer 1 and 2 are used for the angle control and the torque control, respectively.

as shown in Fig. 3. There is no difference in the placement of potentiometer 1 between the AIRo-5.1 and the AIRo-5.2. However, in the AIRo-5.1, potentiometer 2 revolves around the middle joint axis; whereas, in the AIRo-5.2, potentiometer 2 does not.

Since the gear ratio between potentiometer 1 and the joint shaft is $R_1(=1.6)$, the rotation angle around the middle joint axis by the joint motor ($\theta_{3\,\mathrm{in}}$) is defined as follows:

$$\theta_{3\,\mathrm{in}} = \psi_1 / R_1 \tag{1}$$

where ψ_1 denotes the measured angle of potentiometer 1. In a similar way, the actual joint angle (θ_3) is measured by

$$\theta_3 = \psi_2 / R_2 \tag{2}$$

where ψ_2 and R_2 denote the measured angle of potentiometer 2 and the gear ratio between potentiometer 2 and the joint shaft, which is $R_2 = 2.5$, respectively.

The angular displacement of the polyurethane rubber spring ($\Delta\theta_e$) can be derived by

$$\Delta\theta_e = \theta_{3\,\mathrm{in}} - \theta_3. \tag{3}$$

Multiplying $\Delta\theta_e$ by its rotational stiffness (K_e) gives the middle joint torque (τ_3). Therefore, the value of τ_3 can be then calculated by

$$\tau_3 = K_e \Delta\theta_e. \tag{4}$$

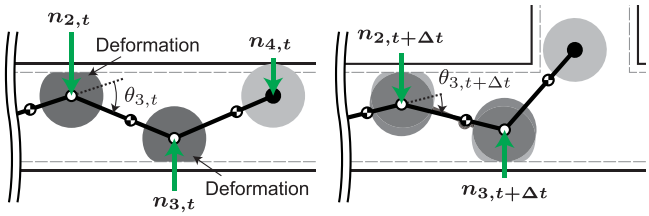

Fig. 4. Principle of joint angle change when encountering T-branches: static equilibrium at the time of t (a) and that at the time of $t + \Delta t$.

III. REQUIREMENTS FOR AUTOMATIC T-BRANCH TRAVEL

As proposed in [24], the middle joint angle needs to be controlled along a cosine trajectory to pass through a T-branch. However, the joint is torque-controlled in the straight section, and it is necessary to switch to angle control once the robot enters the T-branch. Here, the change of the middle joint angle is analyzed based on the partial dynamic model of the robot at T-branches. From this result, the threshold of angle change to use as a trigger for switching the control mode automatically is determined.

Because the amount of change in the joint angle is focused upon, it is available for straight pipes with different inner diameters. A threshold is set for this angle change, and when the value is exceeded, the control target is shifted from the joint torque to the joint angle. After the T-branch travel is completed, the system returns to torque control. This function can be achieved most simply by attaching an angle sensor to the head the joint instead of the middle one. Adding additional sensors and microcontrollers to communicate with them, however, is impractical for in-pipe robots of very limited size.

Fig. 4 illustrates the principle of the angle value change when the robot encounters T-branches. At time t, when the robot is statically balanced in a straight pipe, a normal force is applied to the end of each link, as shown in Fig. 4(a). Once only link 4 enters the T-branch, and the contact between the wheel and the inner wall of the pipe is broken, the magnitudes of the normal forces $\boldsymbol{n}_3$ and $\boldsymbol{n}_2$ decrease, as shown in Fig. 4(b). In Fig. 4(a), a large force is applied to the omni-wheel due to the middle joint torque τ_3 and the spring torque of the head joint τ_4, causing the rubber part of the wheel to deform. However, as shown in Fig. 4(b), if the normal force decreases, the joint angle closes slightly due to the restoring force of the rubber, even though the joint torque is controlled to maintain a constant value. By utilizing this change as a trigger to switch from torque control to angle control, automatic T-branch travel is realized.

A. Partial Dynamic Model of the Robot During the Early Stage of T-Branch Travel

To elucidate the physical phenomena described above, in this section, the equations of motion are defined that take into account the dynamic effect of only link 4, and the relationship between

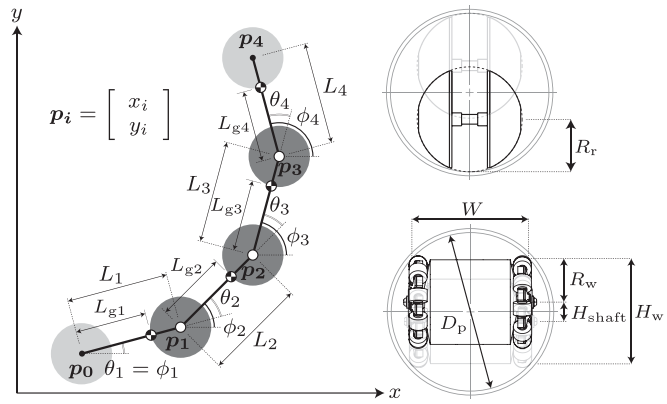

Fig. 5. Kinematic model of the robot and the parameters used to calculate the joint angle trajectory.

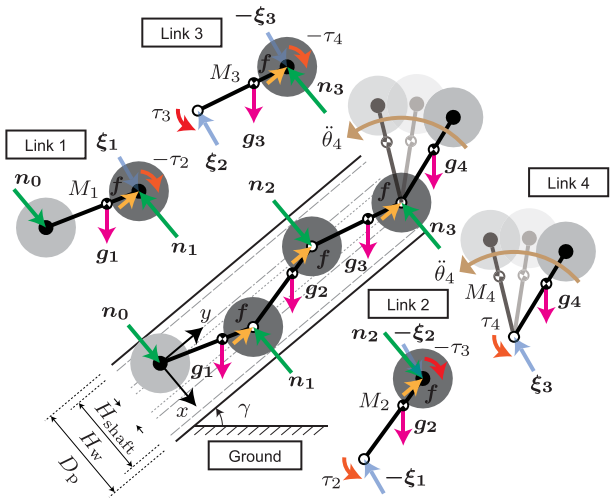

Fig. 6. Partial dynamic model of the four-link in-pipe robot when only link 4 breaks the contact.

the change in the middle joint angle and the hardware parameters of the robot is discussed.

As in [22], a kinematic model of a 4-link in-pipe inspection robot is shown in Fig. 5. L_i and L_{gi} denote the ith link length and the length between the end of each link and each center of gravity, respectively (both are constant). θ_i and ϕ_i mean the ith relative joint angle and absolute posture angle in the xy-coordinate system, respectively. $D_\mathrm{p}, W, R_\mathrm{w}, R_\mathrm{r}, H_\mathrm{w}$, and H_shaft denote the inner pipe diameter, the width between a pair of the drive wheel (omni-wheels), the radius of the drive wheel, the radius of the spherical wheel, the space where the drive wheels can move within, and the space where the drive shaft can move within, respectively.

Fig. 6 shows the partial dynamic model of the robot when only link 4 breaks the contact. To increase generality, the pipe is assumed to be inclined by γ from the ground. The gravitational acceleration g is assumed to be applied vertically downward to the ground. The origin of the xy-coordinate system is placed at the base of the robot ($\boldsymbol{p}_0 = [0\ 0]^\mathrm{T}$), and the y-axis is set to be parallel to the pathway direction of the pipe.

$\boldsymbol{n}_i, \boldsymbol{f}, \boldsymbol{g}_i, \boldsymbol{\xi}_i, M_i$, and τ_i denote a vector of ith normal force, a vector of ith driving force of the wheel (tangential direction), a vector of ith gravity force, and a vector of internal force applying between two adjacent links, and mass of ith link, and joint torque of the ith link, respectively.

$$\boldsymbol{n}_i = n_i \boldsymbol{e}_{\mathrm{n}i},\ (i = 0, 1, 2, 3, 4) \tag{5}$$

$$\boldsymbol{f} = f \boldsymbol{e}_{\mathrm{t}i},\ (i = 1, 2, 3) \tag{6}$$

$$\boldsymbol{g}_i = \begin{bmatrix} M_i g \cos\gamma & -M_i g \sin\gamma \end{bmatrix}^\mathrm{T},\ (i = 1, 2, 3, 4) \tag{7}$$

where $\boldsymbol{e}_{\mathrm{n}i}$, $\boldsymbol{e}_{\mathrm{t}i}$, n_i, f, and g denote the unit vectors of the ith normal and tangential driving forces, absolute value of the ith normal force, absolute value of the drive force, and gravity acceleration, respectively. It is assumed that f is distributed and applied evenly to each drive wheel.

The equation of motion of the robot when only the head wheel leaves the pipe wall is given by

$$\mathbf{M}\ddot{\boldsymbol{q}} + \boldsymbol{h} + \mathbf{D}\dot{\boldsymbol{q}} = \boldsymbol{\tau} + \boldsymbol{g} + \mathbf{B}\boldsymbol{\lambda} \tag{8}$$

where $\mathbf{M} \in \Re^{6\times6}$, $\boldsymbol{h} \in \Re^{6\times1}$, $\mathbf{D} \in \Re^{6\times6}$, $\boldsymbol{\tau} \in \Re^{6\times1}$, $\boldsymbol{g} \in \Re^{6\times1}$, $\mathbf{B} \in \Re^{6\times6}$, and $\boldsymbol{\lambda} \in \Re^{6\times1}$ denote an inertia matrix of the robot, a vector due to centrifugal and Coriolis forces, a diagonal matrix due to viscosity, a vector of joint torques generated by the torsional springs and motor, a vector of force in x- and y-axis directions and joint moments generated by gravity, a matrix used to convert the tangential and normal forces on the wheel axle to the x- and y-axis directions and the dimension of rotation, and a vector consisting of normal force (constraint force) and tangential force (driving force) applied to the wheel axle, respectively.

The generalized coordinates $\boldsymbol{q} \in \Re^{6\times1}$ are contained in a vector $\boldsymbol{q} = [x_0\ y_0\ \theta_1\ \theta_2\ \theta_3\ \theta_4]^\mathrm{T}$.

From (8), the equation of motion for the rotation of link 4 [the same as solving the sixth row of (8)] can be described as follows:

$$\ddot{\theta}_4 = \frac{K\Theta_{\mathrm{nat}4} - K\theta_4 - D_6\dot{\theta}_4 - M_4\, g L_{g4} \sin(\phi_4 + \gamma)}{I_4} \tag{9}$$

where K, Θ_nat, and D_6 denote the spring stiffness and the natural angle of the torsion spring, and the rotational viscosity of link 4 around the head joint, respectively.

$I_{\mathrm{G}4} + M_4 L_{g4}^2$ is replaced by I_4, which means the inertia moment of link 4 around the head joint (endpoint). Now, the angular acceleration of the head joint as the differential equation of a simple second-order delay system has been defined. By solving this numerically as an ordinary differential equation, the angular velocity and angle of the joint can also be derived.

From the fifth row of (8), the equations of motion for link 3 can be redescribed by

$$n_3 = \frac{1}{L_3 \sin\phi_3}\Big\{\tau_4 - \tau_3 + M_4 L_3 L_{g4}(\ddot{\theta}_4 \cos\theta_4 - \dot{\theta}_4^2 \sin\theta_4) + (M_3 L_{g3} + M_4 L_3) g \sin(\phi_3 + \gamma) + f L_3 \cos\phi_3 \Big\} \tag{10}$$

where τ_3 is the controllable torque of the middle joint which is commanded manually. Originally, the components of the sixth

TABLE II
INITIAL PARAMETERS FOR THE PARTIAL DYNAMIC SIMULATION

D_{p} [m]	0.104	L_{g2} and L_{g3} [m]	0.06
R_{w} [m]	0.03	M_1 and M_4 [kg]	0.426
R_{r} [m]	0.0325	M_2 and M_3 [kg]	0.815
W [m]	0.076	γ [deg]	0
L_1 and L_4 [m]	0.125	K [Nm/deg]	0.0116
L_2 and L_3 [m]	0.1	Θ_{nat4} [deg]	112
L_{g1} [m]	0.056	I_4 [kgm^2]	0.002962
L_{g4} [m]	0.064	Sampling time [s]	0.0001

row were included, and thus they are grouped together as τ_4. f can also be derived from the second row of (8)

$$f = \frac{M_4 L_{\mathrm{g4}}(\ddot{\theta}_4 \cos\phi_4 - \dot{\theta}_4^2 \sin\phi_4) + Mg\sin\gamma}{3}. \tag{11}$$

Essentially, this value of τ_3 is known since it is given as the target value of the middle joint torque. Therefore, only n_3 is unknown and can be solved for.

B. Verification of Joint Angle Change by Simulation

In this section, how n_3 changes with respect to time from the moment when the head wheel of link 4 detaches from the pipe wall is examined. Table II lists the initial parameters for the partial dynamic simulation. I_4 and L_{g4} are obtained from a function of the CAD that automatically calculates the center of gravity and moment of inertia. The Euler method, as an ordinary differential equation, was used for numerical integration. However, D_6 is unknown and very hard to determine. From the basics of damping and vibration dynamics, the viscosity coefficient during critical damping in the condition without gravity D_{cr6} can easily be derived by $D_{\mathrm{cr6}} = 2\sqrt{I_4 K}$. Substituting the values listed in Table II to this resulted in $D_{\mathrm{cr6}} = 0.089$ Nms/rad. Even if the horizontal link 4 of the real robot is manually moved by hand, it is obvious that no vibration phenomenon is observed. Therefore, it can be concluded that at least the actual D_6 is greater than at least 0.089 Nms/rad.

At $D_{\mathrm{cr6}} = 0.089$ Nms/rad, θ_4 is critically damped if there is no gravity. However, since n_3 is still subject to oscillatory phenomena and the influence of gravity, D_6 must be set to a larger value than D_{cr6}. In this study, $D_{\mathrm{cr6}} = 0.1$ Nms/rad is selected for the simulation, which suppresses the vibration phenomenon.

Fig. 7 shows the effect of n_3 on the pipe tilt angle γ relative to the ground. When $\gamma = 0$ deg, the pipe is horizontal, and gravity disturbs the rotation of link 4. This corresponds to the gravity term in (9). As a result, the value of $\ddot{\theta}_4$ is small, and the normal force change is the smallest at $\gamma = 0$ deg. To detect the T-branch by the threshold of the joint angle value, the larger the change is in normal force n_3, the easier it is to detect. In this study, the most severe conditions at $\gamma = 0$ deg were simulated.

Figs. 8 and 9 plot the simulated normal force transition n_3 with different spring stiffness K where $\gamma = 0$ deg, $\Theta_{\mathrm{nat4}} = 112$ deg, and $D_6 = 0.1$ Nms/rad and that with different natural angle of the spring $\gamma = 0$ deg, Θ_{nat4} where $K = 0.0116$ Nm/deg and $D_6 = 0.1$ Nms/rad, respectively. In all cases, n_3 eventually converges to approximately 21 N. This means that the head

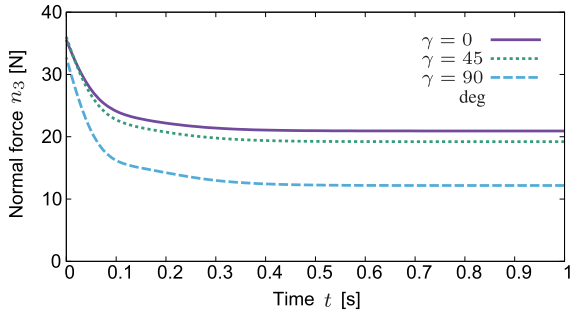

Fig. 7. Simulated normal force n_3 with different tilted angle of the pipe γ, where $K = 0.0116$ Nm/deg, $\Theta_{\mathrm{nat4}} = 112$ deg, and $D_6 = 0.089$ Nms/rad.

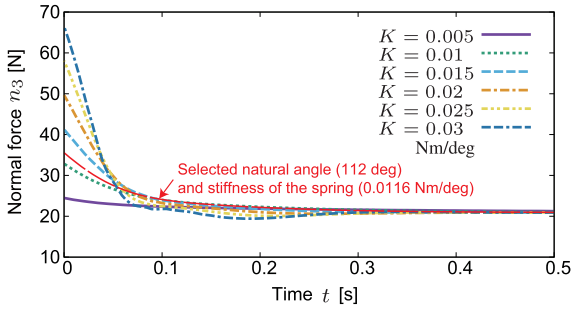

Fig. 8. Simulated normal force n_3 with different spring stiffness K, where $\gamma = 0$ deg, $\Theta_{\mathrm{nat4}} = 112$ deg, and $D_6 = 0.1$ Nms/rad.

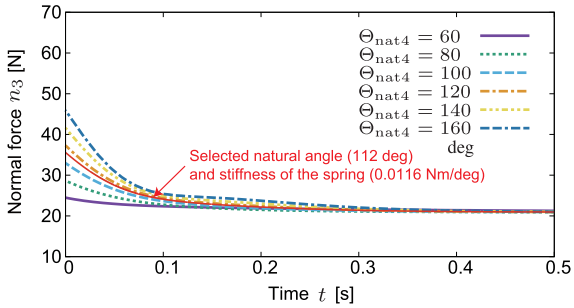

Fig. 9. Simulated normal force n_3 with different natural angle of the spring Θ_{nat4}, where $\gamma = 0$ deg, $K = 0.0116$ Nm/deg, and $D_6 = 0.1$ Nms/rad.

spherical wheel has left the inner wall of the pipe, and the effect of the normal force due to τ_4 has completely disappeared.

To detect the change of the middle joint angle correctly, a large normal force change is required so that it is not lost in the noise. Therefore, from Figs. 8 and 9, both the stiffness and the natural angle of the spring should be designed to be large. However, due to the limited space in the joint, the spring cannot be chosen freely in practice; in general, to increase the stiffness, the wire diameter needs to be increased, and to increase the natural angle, the number of turns needs to be increased.

In this study, these compromises were selected from the specifications of the torsional spring. The wire diameter, coil inner diameter, number of turns, and usable angular range of the torsion spring used in the AIRo-5.2 are 0.0023 m, 0.018 m,

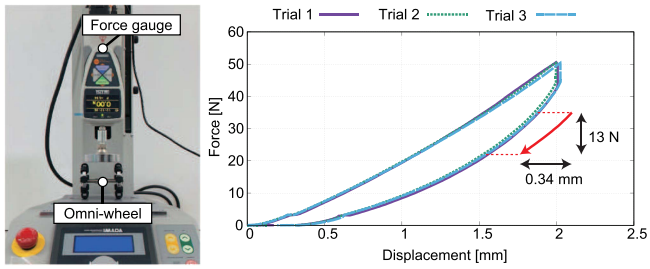

Fig. 10. Measured stiffness of the omni-wheel.

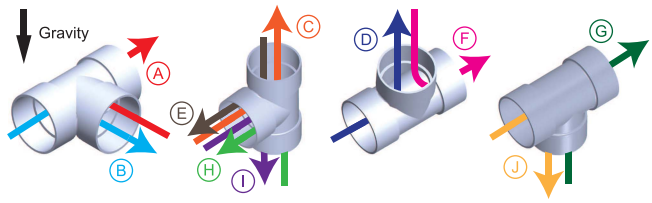

Fig. 11. Different types of the T-branch pathway for the experiments.

6 turns, and 103 deg, respectively. During the T-branch travel, the angles of the front and rear joints need to change from 9 deg at minimum to 85 deg at maximum. Therefore, linear stiffness is guaranteed up to 103 deg starting at 9 deg. The natural angle was then chosen at $\Theta_{\mathrm{nat4}} = 112$ deg, and this corresponds to a spring stiffness of $K = 0.0116$ Nm/deg. In practice, however, the joint angles may exceed this range. In particular, when it is below 9 deg, linearity is not guaranteed. Furthermore, when it is much lower than this, plastic deformation may occur, requiring a stopper or something.

On the other hand, the damping curves plotted in Figs. 8 and 9 show that for the natural angle and stiffness chosen in this study, the normal force n_3 decreases from approximately 35.5 to 22.2 N in the time range of $t = 0$ to $t = 0.2$ s. This corresponds to an approximately 91% decrease in the normal force change of the total interval $t = 0$ to $t = 1$ s. Therefore, in this study, it is assumed that the change in the middle joint angle is detected by using the decrease in the normal force between the time that the robot reaches the T-branch and $t = 0.2$ s.

The relationship between the normal force n_3 and the middle joint angle θ_3 depends on the stiffness of the wheel rubber. For this reason, the displacement and force are measured by pressing the same wheel as the one actually used for the robot, with a plate attached to the tip of a force gauge ZTA-50 N (Imada Co., Ltd., Toyohashi, Aichi, Japan). Fig. 10 shows a picture of the test rig (left) and the measured results of three trials (right). From the experiment, it was revealed that a force of approximately 50 N was generated when the wheel was pushed 2 mm.

From the above simulation, it was expected that at the natural angle and stiffness chosen in this study ($\Theta_{\mathrm{nat4}} = 112$ deg and $K = 0.0116$ Nm/deg), n_3 decreases approximately 13 N (from 35.5 to 22.2 N) in the time range of $t = 0$–0.2 s. This corresponds to the wheel rubber restoration of 0.34 mm, as shown in Fig. 10. Since two omni-wheels are attached at both ends ($\boldsymbol{p_2}$ and $\boldsymbol{p_3}$) for link 3 (in a strict sense, four wheels), this change is doubled to 0.68 mm. Therefore, when the head of the robot enters the T-branch, the parameter H_{shaft} should change as $H_{\mathrm{shaft3},t+\Delta t} = H_{\mathrm{shaft3},t} - 0.00068$ m at link 3. However, it should change as $H_{\mathrm{shaft2},t+\Delta t} = H_{\mathrm{shaft2},t} - 0.00034$ m at link 2, since the wheel rubber restoration at $\boldsymbol{p_2}$ only is applied. $H_{\mathrm{shaft}i,t}$ denotes the value of H_{shaft} at ith link and at time t. Initial value of H_{w} and H_{shaft} can be calculated as 0.071 and 0.016 m, respectively, by D_{p}, R_{w}, and W based on our previous work [24]. Consequently, from [22], joint angle change $\Delta\theta_3$ can be derived by

$$\begin{aligned}\Delta\theta_3 &= \theta_{3,t+\Delta t} - \theta_{3,t} \\ &= \phi_{3,t+\Delta t} - \phi_{2,t+\Delta t} - (\phi_{3,t} - \phi_{2,t}) \\ &= \cos^{-1}\frac{H_{\mathrm{shaft3},t+\Delta t}}{L_3} - \cos^{-1}\frac{H_{\mathrm{shaft2},t+\Delta t}}{L_2} \\ &\quad - \left(\cos^{-1}\frac{H_{\mathrm{shaft3},t}}{L_3} - \cos^{-1}\frac{H_{\mathrm{shaft2},t}}{L_2}\right). \end{aligned} \tag{12}$$

Substituting the parameters listed in Table II to (12), the resultant $\Delta\theta_3$ was approximately 0.59 deg. From (2), this is multiplied by the reduction ratio of $R_2 = 2.5$, and thus the change in potentiometer 2 is $\Delta\psi_2 = 1.48$ deg.

IV. Experiments

Since the T-branch has three intersecting pathways, a variety of routes exist, depending on the pattern of entrances and exits and the direction of gravity. Therefore, in this experiment, 10 different courses were prepared, as shown in Fig. 11. Ⓐ and Ⓑ are both horizontal T-branch pipes. The difference is whether the robot enters the main line from the branch section or from the main line to the branch section. In other words, the difference is whether or not there is a wall in front of the robot. In general, entering the branch section from the main line (Ⓑ, Ⓓ, Ⓔ, Ⓗ, Ⓙ) are more difficult. This is because the wheels cannot make contact with the inner wall of the pipe in front of the robot, and thus cannot generate sufficient propulsive force.

A. Two Types of Controllers

1) Controller for the Middle Joint Angle: From the target angle of the middle joint to be controlled ($\theta_{3\mathrm{d}}$), the target value of potentiometer 2 ($\psi_{2\mathrm{d}}$) can be obtained directly as follows:

$$\psi_{2\mathrm{d}} = R_2\theta_{3\mathrm{d}} \tag{13}$$

Thereby, the control input (v) to the joint motor is simply given by the PID control law

$$v = K_{\theta\mathrm{p}}(\psi_{2\mathrm{d}} - \psi_2) - K_{\theta\mathrm{d}}\dot{\psi}_2 + K_{\theta\mathrm{i}}\int_0^t (\psi_{2\mathrm{d}} - \psi_2)\delta s \tag{14}$$

where $K_{\theta\mathrm{p}}$, $K_{\theta\mathrm{d}}$, $K_{\theta\mathrm{i}}$, and δs denote the proportional gain, the derivative gain, the integral gain, and the infinitesimal time (sampling time) for the joint angle controller, respectively.

2) Controller for the Middle Joint Torque: Since the middle joint of the present robot is equipped with a SEA, its torque

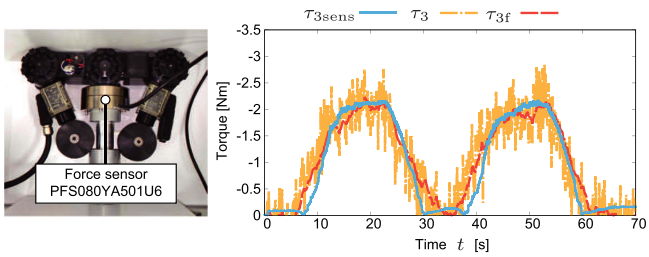

Fig. 12. Torque measured by the force sensor and the embedded SEA.

control is essentially equivalent to the control of the deformation angle of the polyurethane rubber spring. This control of the amount of deformation angle of the rubber spring can be achieved by controlling the angle of potentiometer 1 by adding the amount of the target deformation angle (τ_{3d}/K_e) to the middle joint angle measured by potentiometer 2 (ψ_2/R_2). Therefore, the target angle of potentiometer 1 (ψ_{1d}) can be defined by

$$\psi_{1d} = R_1 \left(\frac{\psi_2}{R_2} + \frac{\tau_{3d}}{K_e} \right) \tag{15}$$

where τ_{3d} denotes the target value of the middle joint torque. In this experiment, the control input to the motor is given by the following PI control equation:

$$v = K_{\tau p}(\psi_{1d} - \psi_1) + K_{\tau i} \int_0^t (\psi_{1d} - \psi_1)\delta s \tag{16}$$

where $K_{\tau p}$ and $K_{\tau i}$ denote the proportional gain and the integral gain for the joint torque controller, respectively.

B. Verification of Torque Control Performance

If K_e is known, the joint torque of the AIRo-5.2 can be controlled theoretically by (16). However, to confirm whether the torque was really controlled, the actual torque value was measured using a force sensor PFS080YA501U6 (Leptrino Inc., 328-1 Hirahara, Komoro, Nagano, Japan). Fig. 12 shows the experimental setup (left) and torque measurement results (right). True joint torque (τ_{3sens}) measured by the force sensor is calculated by the static equilibrium and the measured real force (F_{sens}) as $\tau_{3sens} = F_{sens} L_2/2$. τ_3 and τ_{3f} denote the joint torque measured by our developed SEA and its simple RC-filtered value with a cutoff frequency of 2.21 Hz, respectively. Here, τ_{3d} was changed from 0 to -2 Nm twice in the measurement.

In our previous study [24], the stiffness of the polyurethane rubber spring was measured as 0.431 Nm/deg. However, the resultant stiffness for the AIRo-5.2 was 0.32 Nm/deg due to individual differences. Thereby, $K_e = 0.32$ Nm/deg was applied for actual joint torque control. From τ_{3sens} and τ_{3f} plotted in Fig. 12, the SEA is working well, and the joint torque is accurately controlled.

C. Automatic T-Branch Travel Strategy

1) Trajectory of the Middle Joint Angle: The trajectory of the middle joint angle with respect to time was discussed in our previous work [24], and it is given by

$$\theta_3 = -\alpha \cos \omega t + \beta \tag{17}$$

where α, ω, and β denote the amplitude, angular frequency, and offset of the cosine trajectory, respectively.

$\alpha = 40.29$ deg, $\omega = 0.91$ rad/s, and $\beta = 21.88$ deg were chosen according to [24]. However, these are the values at the moment when the wheels contact the inner wall of the pipe, and thus the normal force is zero. In practice, by providing an angular trajectory in which the middle joint does not bend too much, T-branch travel can be achieved while pressing the wheels against the inner wall of the pipe. In other words, if the maximum value of θ_3 ($\theta_{3,max} = \alpha + \beta$) is as large as the conventional value of 62.17 deg, the head omni-wheel will slip more easily. In our experiments, therefore, $\alpha = 35$ deg and $\beta = 15$ deg were set so that $\theta_{3,max}$ reaches only up to 50 deg.

On the other hand, the value of ω is also not necessarily 0.91 rd/s, since it is just a value that matches the motion speed of the in-pipe robot. Here, $\omega = 1.6$ rad/s was applied for courses Ⓐ through Ⓕ, Ⓘ, and Ⓙ, while $\omega = 1.2$ rad/s was applied only for courses Ⓖ and Ⓗ. This value was determined based on the preliminary experiments and gravity direction considerations.

2) Automatic Switching From Torque Control to Angle Control: For T-branch detection and switching from joint torque control to angle control, the change in potentiometer 2 ($\Delta\psi_{2,j}$) is given by the following equation:

$$\Delta\psi_{2,j} = \psi_{2,j} - \frac{\sum_{k=1}^{j} \psi_{2,k}}{j} \tag{18}$$

where j denotes the number of sampling after starting the algorithm for automatic T-branch travel. The second term in (18) represents the moving average to eliminate the influence of noise. Therefore, $\Delta\psi_{2,j}$ is defined by the difference between the jth angle of potentiometer 2 ($\psi_{2,j}$) and its average during j times. If the computer acquires more than 1 deg of $\Delta\psi_{2,j}$ [this threshold was determined based on the result of (12)], a signal to switch the joint torque control to the joint angle control is sent automatically. To increase the effectiveness of noise reduction, this angle difference discrimination is set to be performed only when $j \geq 10$. Since it is expected to detect the angle change within 0.2 s after the robot head enters the T-branch, the sampling time was set to 0.05 s.

D. Experimental Results

In this study, multiple experiments were conducted per each course, and the number of trials and success rates were examined until five successes were achieved. The robot started the automatic travel algorithm from a position in the straight pipe approximately 0.2–0.3 m away from the junction point of the T-branches. τ_{3d} was set to -1.0 Nm to press the omni-wheels against the inner wall of the pipe.

Fig. 13 shows the experimental video clips during the T-branch travel for all courses and the measured middle joint angle (θ_{3in} and θ_3), middle joint torque (τ_3 and simple *RC* low pass filtered measured middle joint torque τ_{3f}), and angle change of potentiometer 2 ($\Delta\psi_2$) for each, respectively. Here, a simple

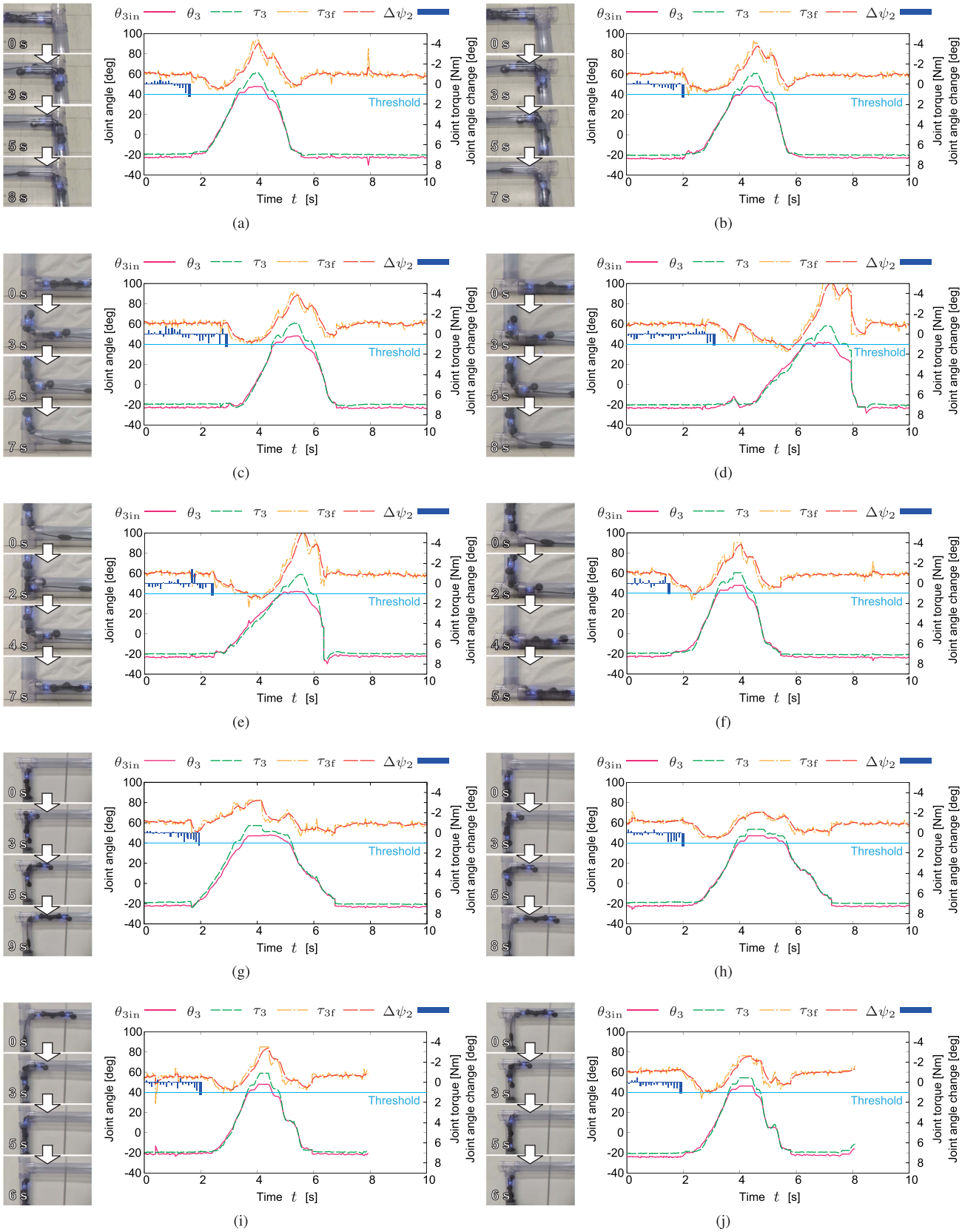

Fig. 13. Measured angles ($\theta_{3\mathrm{in}}$: measured middle joint angle including the deformation of the rubber spring and θ_3: true middle joint angle), torques ($\tau_{3\mathrm{d}}$: target middle joint toque, τ_3: measured middle joint torque, and $\tau_{3\mathrm{f}}$: simple RC low pass filtered measured middle joint torque), and change in the middle joint angle measured as the angle of potentiometer 2 $\Delta\psi_2$ during the automatic T-branch travel experiments: (a) course Ⓐ, (b) course Ⓑ, (c) course Ⓒ, (d) course Ⓓ, (e) course Ⓔ, (f) course Ⓕ, (g) course Ⓖ, (h) course Ⓗ, (i) course Ⓘ, and (j) course Ⓙ.

TABLE III
SUCCESS RATE OF T-BRANCH TRAVEL

Course	Ⓐ	Ⓑ	Ⓒ	Ⓓ	Ⓔ	Ⓕ	Ⓖ	Ⓗ	Ⓘ	Ⓙ
Number of success	5/5	5/6	5/6	5/11	5/6	5/5	5/5	5/7	5/5	5/5
Success rate [%]	100	83	83	45	83	100	100	71	100	100

RC-filtered value with a cutoff frequency of 1.36 Hz was applied to obtain τ_{3f}. The overall success rate is summarized in Table III.

The experimental results showed that the angle change detection of potentiometer 2 worked as expected for Ⓐ, Ⓕ, Ⓖ, Ⓘ, and Ⓙ, and the robot passed through the T-branch very smoothly. The angle change resulted approximately 1 deg and more in the positive direction when the robot entered the entrance of the T-branch, as we expected in the simulation. Similarly, the experiments with Ⓑ, Ⓒ, and Ⓕ failed once, and basically succeeded with high probability. The poorest results were for Ⓓ and Ⓗ, with less than half the success rate for Ⓓ. These failures occurred because the amount of change in potentiometer 2 did not exceed the threshold value of 1 deg.

This problem is highly related to the effect of gravity. Specifically, this means that the gravitational term described in (10) is influenced by γ. For instance, in the Ⓓ experiment with the lowest success rate, even though link 4 enters the T-branch and the normal force n_3 decreases, the rubber of the wheel does not push link 3 up very much because gravity pushes this against the wall. The same phenomenon occurs in the Ⓗ experiment, as well. However, this effect is not as large as that in Ⓓ due to the smaller radius of the moment caused by gravity.

The same phenomenon is likely to occur in the experiment with Ⓒ. However, in the environment of Ⓒ, after link 4 breaks contact, the head omni-wheel moves into the path of the T-branch in the opposite direction of the desired moving direction, which can cause the angle of potentiometer 2 to change significantly and exceed the threshold. This is not the principle for which we originally aimed. It can be effectively used, however, to increase the success rate of the robot's T-branch travel. This is probably the reason for the 100% success rate for all of the remaining courses with a wall in front of the robot: Ⓐ, Ⓖ, Ⓙ, and Ⓕ.

There are several possible ways to increase the success rate in the T-branch where there is no wall in front of the robot. First, the stiffness of the rubber of the wheels should be reduced to increase the amount of recovery relative to the change in the normal force n_3. Depending on the material, this also tends to increase the coefficient of friction, which assists to reduce slippage. However, if the stiffness is reduced too much, the durability of the rubber material generally deteriorates, and thus care must be taken to avoid this.

The second is to increase the amount of change in n_3 by increasing the stiffness or natural angle of the torsion spring. This has already been discussed in Figs. 8 and 9. To achieve this, a larger spring is required, and thus the size constraints of the robot need to be considered. In general, the larger is the spring stiffness, the smaller is the available natural angle. On the other hand, as the available natural angle is increased, the spring stiffness is decreased.

The third is to make the threshold of $\Delta\psi_2$ even smaller than the current 1 deg. However, this comes with the risk of being susceptible to noise. In our experiments, it was found that lowering the threshold to approximately 0.8 deg seemed to be acceptable. If it was lowered further, however, the noise was recognized as exceedance of the threshold, and angle control started for the T-branch travel. Currently, an analog potentiometer is installed as an angle sensor. The signal line for this goes through a very narrow space inside of the robot, along with the motor and power lines. If this can be replaced by a digital encoder, then the noise could be decreased substantially. Subsequently, a smaller threshold may be set. These three solutions are currently under further investigation.

V. CONCLUSION

In this article, an articulated wheeled in-pipe inspection robot with active and passive elastic joints that can travel through vertical T-branch pipes was proposed. The achievements of this study were as follows: first, our robot AIRo-5.2, which can travel on vertical T-branches quickly (within 10 s), targets very narrow pipes with inner diameters of 4 in or less. This may constitute a performance that was already possible with other robots with larger adaptive inner pipe diameters. However, it was very difficult to reduce the size of these robots without diminishing their performance.

In the past, in-pipe robots have existed that can pass through both vertical bent and T-branch pipes with an inner diameter of 4 in or less [27], [28]. However, the T-branches used in their experiments have a large radius of curvature of the inner corner, and not the zero-radius (sharp inner corner) T-branch used in our experiment. Furthermore, the wheels of conventional in-pipe robots were pressed against the inner wall of the pipe only by a spring mechanism, which might not generate sufficient propulsive force to pull a long and heavy cable when traveling long distances. Our robot AIRo-5.2, on the other hand, has an active elastic joint mechanism with a SEA to adjust the normal force applied to its wheels. When the cable needs to be pulled over a long distance without being interrupted by the weight or friction with the wall, the middle joint torque can be increased and move with a strong pulling force.

It should also be mentioned that it is very easy for humans to operate. If the object to be inspected is only straight pipes or bent pipes, only the torque of the middle joint needs to be controlled, and then the omni-wheels can be driven in an open loop for smooth traveling inside of these pipes. If the bending direction of the bent pipe is not aligned with that of the robot's joints, it is necessary to rotate the spherical wheel to adjust the robot posture around the pipe axis, which can easily be done while watching the camera image. The shadow image-based method proposed in our previous work may be also applied [29].

The same is true for the T-branch. As long as the posture is correct, the robot can automatically switch from joint torque control to joint angle control, and pass through the T-branch by activating the automatic travel algorithm just before approaching its corner. The automatic T-travel function could sometimes fail. However, it is possible to return to the initial position and repeat

the trial indefinitely. The SEA inside of the joint mechanically mitigates impact forces, and by monitoring the torque, abnormal external forces can be avoided.

In the future, we will attempt to further reduce the size and weight of the AIRo-5.2, improve its basic performance, such as traction force, and travel longer distances than a few tens of meters. In addition, we will also consider adaptability to uneven environments inside of the pipes due to dirt and corrosion, a method of rescuing the robot in case it becomes stuck inside of the pipes, and dust and waterproofing.

References

[1] H. P. Huang, J. L. Yan, and T.-H. Cheng, "Development and fuzzy control of a pipe inspection robot," *IEEE Trans. Ind. Electron.*, vol. 57, no. 3, pp. 1088–1095, Mar. 2010.

[2] J. Park, D. Hyun, W.-H. Cho, T.-H. Kim, and H.-S. Yang, "Normal-force control for an in-pipe robot according to the inclination of pipelines," *IEEE Trans. Ind. Electron*," vol. 58, no. 12, pp. 5304–5310, Dec. 2011.

[3] A. Kuwada, S. Wakimoto, K. Suzumori, and Y. Adomi, "Automatic pipe negotiation control for snake-like robot," in *Proc. IEEE/ASME Int. Conf. Adv. Intell. Mechatronics*, 2008, pp. 558–563.

[4] D. Rollinson and H. Choset, "Pipe network locomotion with a snake robot," *J. Field Robot.*, vol. 33, no. 3, pp. 322–336, 2016.

[5] S. Xiao, Z. Bing, K. Huang, and Y. Huang, "Snake-like robot climbs inside different pipes," in *Proc. IEEE Int. Conf. Robot. Biomimetics*, 2007, pp. 1–8.

[6] M. Inazawa, et al., "Unified approach to the motion design for a snake robot negotiating complicated pipe structures," *Front. Robot. AI*, vol. 8 pp. 1–18, 2021.

[7] Z. Zhang, X. Wang, S. Wang, D. Meng, and B. Liang, "Design and modeling of a parallel-pipe-crawling pneumatic soft robot," *IEEE Access*, vol. 7, pp. 134301–134317, 2019.

[8] T. Kishi, M. Ikeuchi, and T. Nakamura, "In-pipe inspection robot capable of actively exerting propulsive and tractive forces with linear antagonistic mechanism," *IEEE Access*, vol. 9, pp. 131245–131259, 2021.

[9] T. Yamamoto, S. Sakama, and A. Kamimura, "Pneumatic duplex-chambered inchworm mechanism for narrow pipes driven by only two air supply lines," *IEEE Robot. Automat. Lett.*, vol. 5, no. 4, pp. 5034–5042, Oct. 2020.

[10] S. Kodama et al., "Development of pneumatic driven robot system which can entry and retire from gas pipe," in *Proc. IEEE Int. Conf. Mechatronics Automat.*, 2021, pp. 1466–1471.

[11] E. Rome, et al., "Towards autonomous sewer robots: The MAKRO project," *Urban Water*, vol. 1, pp. 57–70, 1999.

[12] C. Birkenhofer, M. Hoffmeister, J. M. Zollner, and R. Dillman, "Compliant motion of a multi-segmented inspection robot," in *Proc. IEEE/RSJ Int. Conf. Intell. Robots Syst.*, 2005, pp. 2632–2637.

[13] J. Borenstein, M. Hansen, and A. Borrell, "The OmniTread OT-4 serpentine robot-design and performance," *J. Field Robot.*, vol. 24, no. 7, pp. 601–621, 2007.

[14] S. Fjerdingen, P. Liljebäck, and A. Transeth, "A snake-like robot for internal inspection of complex pipe structures (PIKo)," in *Proc. IEEE/RSJ Int. Conf. Intell. Robots Syst.*, 2009, pp. 5665–5671.

[15] H. Schempf, et al., "Visual and nondestructive evaluation inspection of live gas mains using the Explorer^{TM} family of pipe robots," *J. Field Robot.*, vol. 27, no. 3, pp. 217–249, 2010.

[16] H. Jang et al., "Development of modularized in-pipe inspection robotic system: MRINSPECT VII," *Robotica*, vol. 40, no. 5, pp. 1361–1384, 2021.

[17] G. C. Vradis and W. Leary, "Development of an inspection platform and a suite of sensors for assessing corrosion and mechanical damage on unpiggable transmission mains," Technical Report of NGA and Foster-Miller, 2004.

[18] E. Dertien, S. Stramigioli, and K. Pulles, "Development of an inspection robot for small diameter gas distribution mains," in *Proc. IEEE Int. Conf. Robot. Automat.*, 2011, pp. 5044–5049.

[19] P. Debenest, M. Guarnieri, and S. Hirose, "PipeTron series - robots for pipe inspection," in *Proc. 3rd Int. Conf. Appl. Robot. Power Ind.*, 2014, pp. 1–6.

[20] K. Kouno, H. Yamada, and S. Hirose, "Development of active-joint active-wheel high traversability snake-like robot ACM-R4.2," *J. Robot. Mechatronics*, vol. 25, no. 3, pp. 559–566, 2013.

[21] H. Sawabea, et al., "Control of an articulated wheeled mobile robot in pipes," *Adv. Robot.*, vol. 33, no. 20, pp. 1072–1086, 2019.

[22] A. Kakogawa and S. Ma, "Design of a multilink-articulated wheeled pipeline inspection robot using only passive elastic joints," *Adv. Robot.*, vol. 32, no. 1, pp. 37–50, 2018.

[23] K. Tadakuma, "Tetrahedral mobile robot with novel ball shape wheel," in *Proc. 1st IEEE/RAS-EMBS Int. Conf. Biomed. Robot. Biomechatronics*, 2006, pp. 946–952.

[24] A. Kakogawa and S. Ma, "A multi-link in-pipe inspection robot composed of active and passive compliant joints," in *Proc. IEEE/RSJ Int. Conf. Intell. Robots Syst.*, 2020, pp. 6472–6478.

[25] G. A. Pratt and M. Williamson, "Series elastic actuators," in *Proc. IEEE/RSJ Int. Conf. Intell. Robots Syst.*, 1995, pp. 399–406.

[26] D. Rollinson, et al., "Design and modeling of a series elastic element for snake robots," in *Proc. ASME Dynamic Syst. Control Conf.*, 2013, pp. 1–5.

[27] S. Roh and H. R. Choi, "Differential-drive in-pipe robot for moving inside urban gas pipelines," *IEEE Trans. Robot.*, vol. 21, no. 1, pp. 1–17, Feb. 2005.

[28] Y. Kwon and B. Yi, "Design and motion planning of a two-module collaborative indoor pipeline inspection robot," *IEEE Trans. Robot.*, vol. 28, no. 3, pp. 681–696, Jun. 2012.

[29] A. Kakogawa, Y. Komurasaki, and S. Ma, "Shadow-based operation assistant for a pipeline-inspection robot using a variance value of the image histogram," *J. Robot. Mechatronics*, vol. 31 no. 6, pp. 772–780, 2019.

Atsushi Kakogawa (Member, IEEE) received the Ph.D. degree in mechanical engineering from Ritsumeikan University, Shiga, Japan, in 2015.

He joined the Department of Robotics, Ritsumeikan University, Shiga, Japan, as an Assistant Professor, in 2015, as a Lecturer in 2019, and he is currently working as an Associate Professor with Research Organization of Science and Technology, Ritsumeikan University. He was at the University of Waterloo, ON, Canada as a Visiting Assistant Professor, in 2017. His current research interests include the design and control of robots using viscoelasticity and differential mechanisms and robotic in-pipe inspection as an example of snake-like robot applications.

Kenya Murata received the bachelor's degree in engineering from Ritsumeikan University, Shiga, Japan in 2022. He is currently working toward the M.S. degree in engineering with Ritsumeikan University. His research interests include the development and control of in-pipe inspection robots.

Shugen Ma (Fellow, IEEE) received the Dr.Eng. degree in mechanical engineering science from the Tokyo Institute of Technology, Tokyo, Japan, in 1991.

From 1991 to 1992, he was a Researcher with Komatsu Ltd. From 1992 to 1993, he was a Visiting Scholar with the University of California, Riverside, CA, USA. In July 1993, he joined the Department of Systems Engineering, Ibaraki University, Hitachi, Japan, as an Assistant Professor. In October 2005, he joined Ritsumeikan University, Shiga, Japan, where he is currently a Professor with the Department of Robotics. His current research interests include the design and control theory of new types of robots, field robotics, and biorobotics.

Dr. Ma is a Fellow of the Japan Society of Mechanical Engineers and a member of the Society of Instrument and Control Engineers of Japan and the Robotics Society of Japan. He is the General Chair of the 2022 IEEE/RSJ International Conference on Intelligent Robots and Systems. He was an Associate Editor for the IEEE TRANSACTIONS ON ROBOTICS from 2003 to 2007 and an Editor for Advanced Robotics in 2007. He is with many societies and conferences.